Visual space curves before eye movements

Ifedayo-EmmanuEL Adeyefa-Olasupo[1]*

[1]Department of Psychiatry and Psychotherapy, Charité – Universitätsmedizin Berlin

*Berlin School of Mind and Brain, Humboldt-Universität zu Berlin

†Department of Neuroscience, Yale University

ABSTRACT

Despite the incessant retinal disruptions that necessarily accompany eye movements, our percept of the visual world remains continuous and stable – a phenomenon referred to as spatial constancy. How the visual system seamlessly achieves spatial constancy is poorly understood despite almost four centuries worth of theorizing and experimentation (*1-4*). Here, I measured visual sensitivity at geometrically symmetric retinotopic locations, observing transient but marked sensitivity differences between them where none should be observed if cells that support spatial constancy indeed faithfully translate or converge across visual space (*5-10*). These differences, recapitulated by a novel neurobiologically inspired force-field model, reflect an overriding influence of putative visually transient error signals that curve visual space. Intermediate eccentric locations between the current and future location of gaze, likely to contain retinal disruptions are uniquely affected by curved visual space. This suggest that active visual processing at these locations is transiently turned off before an eye movement, and with the gating off of these error signals, fully turned back on after an eye-movement– a proposed novel mechanism underlying spatial constancy.

INTRODUCTION

We rapidly move our eyes, saccade, between two resting locations in space 3 to 5 times per second in order to bring eccentric objects of interest to the central 2° of the visual field (i.e., the fovea) (*11*). Saccades displace our retinal image of the visual world. Yet, we rarely ever notice the retinal disruptions saccades ubiquitously accompany in our day-to-day visual experiences. To account for this visual continuity and stability, early electrophysiological studies posit that cells across retinotopic brain areas predictively shift their spatial extent from their current locations of

sensitivity to their future post-saccadic locations just before a saccade is made. However, it has been long suspected and recently confirmed that these early studies did not sample enough spatial positions to thoroughly assess the reliability of these purely translational retinotopic shifts towards post-saccadic locations (*12*). Specifically, recent electrophysiological studies have uniquely exposed these classical studies and convincingly demonstrate that cells across retinotopic brain areas converge primarily around the eccentric target of the saccade (*8-10*). This has ignited an intense and persistent search of the behavioral correlates that implicates a novel mechanism underlying spatial constancy. To date, no study has been able to provide such an account. Equally unaccounted for is a mechanistic account of the neural computations and architecture that support these behavioral dynamics while preserving retinotopic organization.

RESULTS

Peri-saccadic localization of the eccentric target mirrors initial shifts in gaze but does not mirror later shifts in gaze

Here, human subjects, for the first time, were randomly flashed low-contrast probes for 20ms at 2.5 degrees of visual angle (or dva) from the fixation dot (*Experiment 1*), from the midpoint (at eccentricity of 5°) between the fixation dot and the saccade target (*Experiment 2*), or from the saccade target (*Experiment 3*), at upper and lower tangential locations (i.e., around the path of the saccade, Fig. 1A), geometrically symmetric to one another with respect to the radial axis (i.e., the path the saccade is expected to travel along). To discourage any artificial restriction of visual resources along the tangential axes, probes were also isotropically flashed along the radial axis (See Methods). Subjects reported with a button-press whether they were able to detect a flashed probe around the time of an eye movement towards an eccentric target. With respect to target onset, flashed probes fell within the time window of 0 to 1285ms after target onset (Fig. 1B).

The results in Fig. 2A, 1st panel, calculated across experiments from 0 to 209ms after target onset along the tangential axes show that gaze was unexpectedly averted away from the target in the direction of the foveal tangential clockwise fov_{cw} location. This shift in gaze is agreement with transient increases in neural activity in the posterior parietal cortex during fixation at an eccentric foveal site (*13*). From 210ms to 820ms after target onset (2nd panel) gaze continued to remain eccentric while compressing downward towards the foveal tangential counterclockwise

fov_{ccw} location. This compression in gaze, in anticipation of the saccade, is in part in agreement with the shrinkage of receptive fields observed in the extrastriate cortex (*8, 10*). The spatial distribution between these marked shifts in gaze along radial and tangential axes was statistically significant (rad_{shift}, p = 4.0058e-36; tan_{shift}, p = 0.0149). Fig. 2A, 3rd panel, shows that the saccade landing position, from 0 to 50ms after saccades land in the periphery, was dramatically mislocaized towards the peripheral tangential clockwise $peri_{cw}$ location. This observation, for the first time, explains the orthogonal mislocalization of flashed stimuli away from a stationary target, as observers most likely under these conditions erroneously perceive the eccentric target as tangentially localized (*14, 15*). As expected, a larger variance was observed for the initial locus of gaze (6.84 deg^2) when compared to the variance associated with the compressed locus of gaze (2.12 deg^2). As for the variance associated with the saccade landing position, a larger variance (10 deg^2) was observed when compared to the loci of the gaze in the fovea (Fig. 2A, 4th panel). These results strongly suggest that the tangential bias in the locus of the saccade landing position (more eccentric region) remained mirroring the tangential bias in the initial shift in gaze within the fovea (less eccentric region), even as gaze actively compressed towards the fov_{ccw} location, in turn introducing an angular bearing (curvilinear) component within the representation of visual space.

Curved visual space directly mediates unexpected transient differences in peri-saccadic sensitivity across visual space

To test this "curved visual space" prediction, peri-saccadic sensitivity across visual space were investigated. In line with this prediction, Fig. 2B, 1st panel, shows that when subjects began to compress their gaze downward towards the fov_{ccw} location, there was a transient but marked increase in peri-saccadic sensitivity at the fov_{ccw} location, while at the fov_{cw} location, there was a transient but marked decline in peri-saccadic sensitivity. Indeed, because these retinotopic locations are geometrically symmetric to one another, this should not happen if cells that support spatial constancy faithfully translate or converge (*5-10*). From 820ms onwards after target onset there was a global decline in peri-saccadic sensitivity at both foveal locations. This global decline is in agreement with peri-saccadic corollary discharge commands originating from pre-motor brain areas (*4*). The 2nd and 3rd panels show the opposite pattern in the changes in peri-saccadic sensitivity. Specifically, from 210ms to 820ms after target onset, there are declines in peri-saccadic sensitivity at $para_{ccw}$ and $peri_{ccw}$ locations and increases in peri-saccadic sensitivity at $para_{cw}$

and $peri_{cw}$ locations, which again cannot be explained by a faithful translation or convergent retinotopic shifts across visual space (*5-10*). Equally revealing is the fact that at these eccentric locations, from 820ms onwards after target onset, there is a slow but clear peri-saccadic sensitivity "hand-off", as $para_{ccw}$ and $peri_{ccw}$ locations that once experienced declines in peri-saccadic sensitivity slowly begin to experience increases. Conversely, at $para_{cw}$ and $peri_{cw}$ locations that once experienced increases in peri-saccadic sensitivity slowly begin to experience declines. These peri-saccadic sensitivity hand-offs strongly suggest that curved representations are eventually calibrated around the time a saccade has been planned.

Curved visual space curves trajectories typically expected to travel along a linear path.

To further test this peri-saccadic sensitivity hand-off prediction, saccade trajectories were investigated. In line with this prediction, Fig. 2C shows that trajectories from the current position of gaze towards the periphery were curved across experiments, at a rate of 73% towards the $peri_{cw}$ location, while in 27% of all trials, saccades were curved towards the $peri_{ccw}$ location, reflecting a calibrated visual representation towards the actual location of the target. Specifically, when the saccade target was presented at azimuth angles of 0°, the trajectories were curved towards the per_{cw} location at a rate of 91% with an average curvature of 0.22 in area/amp (*16*). Conversely, for the remaining trials when saccades were curved towards the per_{ccw} location, an average curvature of -0.80 in area/amp was observed. Next, when the peripheral target was presented at an azimuth angle of 45°, the trajectories were curved towards the per_{cw} location at a rate of 65% with an average curvature of 0.56 in area/amp, while for the remaining trials (saccades curved towards the per_{ccw} location) an average curvature of -0.74 in area/amp was observed. Finally, when the saccade target was presented at an azimuth angle of 315°, trajectories were curved towards the per_{cw} location at a rate of 60% with an average curvature of 1.12 in area/amp, while for the remaining trials (saccades curved towards the per_{ccw}) location) an average curvature of -1.17 in area/amp was observed.

Delta-rhythmicity known to support the inhibition of attentional signals support transient differences in peri-saccadic sensitivity

Fig. 3A, 1st panel, shows that a large part of the observed changes in peri-saccadic sensitivity at fov_{cw} and fov_{ccw} locations is actively meditated by rhythmicity in the delta frequency band at ~2 Hz and ~3 Hz respectively, which is known to support attentional signals or, in the case of a lower frequency (~2 Hz), their inhibition during demanding visuomotor tasks (*17*). Fig. 3A, 2nd panel, shows that the spectral signature that mediated the fov_{ccw} location was not location-specific when compared to shuffled data sets (p=0.2280). Conversely, the spectral signature that supported the fov_{cw} location (the locus shifts in gaze was biased towards and away from) was specific to that retinotopic location (p=0.0230). The $para_{cw}$, $para_{cw}$, $peri_{ccw}$, and $peri_{ccw}$ locations also exhibited rhythmicity in the ~2 Hz delta frequency band (Fig. 3B–C, 1st panel). The spectral signature observed at eccentric clockwise and counterclockwise retinotopic locations were not location-specific (p=0.0915, p=0.9725, p=0.3179, p=0.9725) (Fig. 3B–C, 2nd panel). Furthermore, the phase of ~2 Hz within $para_{cw}$ and $para_{ccw}$ locations was consistently offset by approximately 201°, and even larger offset of 290° was observed at the more eccentric $peri_{cw}$ and $peri_{ccw}$ locations (Fig. 3B–C, 3rd panel). This antiphase periodicity at ~2 Hz suggests that the retinotopic brain areas that support these upper and lower eccentric tangential locations are synchronized by attentional dynamics at a common frequency but with location-specific phases (*18*).

Novel neurobiologically inspired retinotopic lever under an inverse force field can explain transient differences in peri-saccadic sensitivity

To provide a mechanistic account of the neural computations and architecture that support this "curved visual space", a neurobiologically inspired phenomenological mechanical model is proposed. At its core, the model assumes that underlying peri-saccadic attentional and oculomotor signals (Fig.3) are actively modulated by what I have termed "visually transient error signals" that is foveal-specific (Fig3A, 1st panel), which give rise to an input and output forces exerted by corresponding time varying masses (Fig. 4B, Fig. 4E) that act upon a "retinotopic lever". Under an inverse force field (ε = -0.55), input and output forces transiently shift spring-loaded sensors – population retinotopic receptive fields (pRFs) that tile visual space and thereby shape normalized density (putative population sensitivity) at a sampled retinotopic location in time (Fig. 4A, Fig. 4D, and Extended Data Fig. 1-2).

As far as the foveal simulations, location-specific visually transient error signals (Fig. 3A) give rise to an input force that is preparing to act on the input arm of a "retinotopic lever" which

158 causes pRFs to shift upper ward in the direction of the fov_{cw} location and later compress towards
159 the fov_{ccw} location (Fig. 2A, 1st and 2nd panel). A compressed input force causes the lever to pivot
160 on its "foveal fulcrum" thereby providing a transient neural advantage at the fov_{ccw} location. To
161 always maintain retinotopic organization, pRFs that tile the more eccentric regions in visual space
162 are initially restricted from over-translating towards the foveal $\mathrm{fov_{cw}}$ location by their population
163 elastic fields (pEFs, see Methods) which remains mirroring the onset location of the input force
164 before a full compression occurs. For the sake of simplicity, foveal simulations began from the
165 point in time when pRFs mirrored the initial shift in gaze (translational output force), followed by
166 late compressive shift towards the fov_{ccw} location (compressed input force) (Fig. 4B). Under these
167 input and output forces, simulation results in Fig. 4C show that putative population sensitivity
168 recapitulated signatures in peri-saccadic sensitivity in the foveal region of visual space (Fig. 2B,
169 1st panel). Assuming that retinotopic cells are not mediated by visually transient error signals (i.e.,
170 visual representation does not include a curved component), translational shifts anticipating retinal
171 image disruptions should have yielded no difference in putative population sensitivity (Fig. 4C,
172 dotted marker) in comparison to peri-saccadic sensitivity observed in Fig. 2B, 1st panel. Similarly,
173 symmetrically convergent retinotopic shifts towards a stationary peripheral site (Fig. 4C, thin
174 markers) cannot explain the changes in peri-saccadic sensitivity observed in the fovea.

175 As far as the eccentric simulations (Fig. 4D), after a fully compressed input force, pRFs
176 moved further towards the fov_{ccw} location in proportion to the mislocalization of the target. Cells
177 across retinotopic brain areas can receive both convergent and translational signals around the time
178 of a saccade (*6, 9*). To this end, pRFs later converged around an emerging output mass which
179 exceeded the magnitude of the initial shift in gaze and approximated the location of the
180 mislocalized target (Fig. 2A, 1st and 3rd panel) (*19*). This is immediately followed by the onset of
181 a translational force proportional to the magnitude of a saccade orthogonal to the radial axis
182 towards the $peri_{cw}$ location (Fig. 4E). Indeed, under three forces, especially when the forces that
183 corresponds to convergent and translational signals emerge, a neural advantage at eccentric
184 clockwise locations should be observed. As predicted, Fig. 4F shows that putative population
185 sensitivity was able to recapitulate peri-saccadic sensitivity signatures at parafoveal locations (Fig.
186 2B, 2nd panel). These simulation results, for the first time, provides a mechanistic account of the
187 neural computations and architecture that supports peri-saccadic retinotopic shifts orthogonal to
188 the saccade direction (*7, 8*). Finally, as expected, a purely translational or symmetrically
189 convergent retinotopic shifts cannot explain changes in peri-saccadic sensitivity.

DICUSSION

Curved visual space is the most fundamental peri-saccadic representation of visual space and can elucidate a range of previously unexplained transient peri-saccadic effects

Overall, results reported here strongly suggest that peri-saccadic retinotopic shifts reflect an overriding influence of visually transient error signals that curves visual space and are not the result of purely translational or convergent signals as previous studies had suggested (*5-10*). Indeed, this is the first time such an observation has been made. Quite convincingly, curved visual space constitutes the most fundamental peri-saccadic representation of visual space and in turn determines (i.) whether a flashed stimuli will be orthogonally mislocaized away from a stationary saccade target (*14, 15*), (ii.) whether cells in the extrastriate cortex will align with or shift orthogonally to the saccade direction (*7, 8*) and (iii.) the extent retinotopic cells will asymmetrically or symmetrically converge towards the saccade target (*20*).

Proposed novel mechanism underlying spatial constancy and its possible predation origins

Most importantly, curved visual space proposes a novel mechanism underlying spatial constancy. Specifically, observed foveal shifts in gaze strongly suggest that the visual system, before saccades, intentionally (mis)directs visual resources in the direction of gaze (i.e., away from retinotopic locations that lie between the presaccadic and post-saccadic retinal locations). These resources are further withheld via retinotopic compressions within the foveal region of visual space which enhances visual process towards the tangential counterclockwise location. In light of this transient opponent (mis)direction and the compression of visual resources, intermediate eccentric regions that were once actively supported by the visual system are no longer so (i.e., visual processing is transiently turned off). This causes visual processing within these regions to significantly lag behind, as it is observed in the behavioral, and computational readouts highlighted above (Fig 2A, 1st, 2nd, 3rd panel; Fig 2B; Fig 2C). Furthermore, because peri-saccadic resources spread across visual space in an extremely slow manner (21), marked here for example by delta rhythmicity (~2 Hz) known to support the inhibition of visual resources (Fig 3), reverted translational spreading of visual resources back towards intermediate eccentric locations is left trailing behind the rapid movement of the eye. This intrinsic difference in speed ultimately allows

the incessant retinal disruptions that necessarily accompany eye movements to escape our day-to-day percept of visual world.

Keeping in mind that Helmholtz, the first researcher to empirically investigate spatial constancy, often referred to this phenomenon as somewhat of a magic trick (2), it is quite remarkable that the human visual system has evolved to account for these retinal disruptions using a (mis)directional strategy, tactic typically used by magicians to manipulate the perception of an observer in order to keep their subtle movements concealed (22). As to the reasons behind the election of such a strategy to achieve spatial constancy, because humans were once preys, one possibility is that it reflects an evolutionarily conversed visuomotor avoidance or escape strategy the mammalian visual system frequently used to track a distal target (e.g., conspecific, predator) from a safe distance (e.g., corner of the eye), which is later followed by a calculated movement (e.g., saccade) towards the location once avoided (*23-25).*

REFERENCES

1. Descartes, R. *Traité de l'homme* (Paris, France, 1644).

2. Helmholtz, H.V. *A treatise on physiological optics* (Dover, New York, NY, 1962).

3. von Holst, E., Mittelstaedt, H. The reafferent principle: reciprocal effects between central nervous system and periphery. *Naturwissenschaften*, 37, 464–476. (1950).

4. Sperry, R.W. Neural basis of the spontaneous optokinetic response produced by visual inversion. *J. Comp. Physiol. Psychol*, 43, 482–489. (1950).

5. Duhamel, J. R., Colby, C. L., Goldberg, M. E. The updating of the representation of visual space in parietal cortex by intended eye movements. *Science*, 255(5040), 90–92. (1992).

6. Umeno, M.M., Goldberg, M.E. Spatial processing in the monkey frontal eye field. I. Predictive visual responses. *J Neurophysiol*, 78:1373–138. (1997).

7. Connor, C. E., Gallant, J. L., Preddie, D. C., Van Essen, D. C. Responses in area V4 depend on the spatial relationship between stimulus and attention. *Journal of Neurophysiology*, 75(3), 1306–1308. (1996).

8. Tolias, A. S., Moore, T., Smirnakis, S. M., Tehovnik, E. J., Siapas, A. G., Schiller, P. H. (2001). Eye movements modulate visual receptive fields of V4 neurons. *Neuron,* 29(3), 757–767.

9. Zirnsak, M., Steinmetz, N. A., Noudoost, B., Xu, K. Z., Moore, T. Visual space is compressed in prefrontal cortex before eye movements. *Nature*, 507, 504–507. (2014).

10. Hartmann, T.S., Zirnsak, M., Marquis, M., Hamker, F.H., Moore, T. (2017). Two types of receptive field dynamics in area V4 at the time of eye movements? *Front. Syst. Neurosci*, 11, 1–7.

11. Rayner, K. Eye movements in reading and information processing: 20 years of research. *Psychol. Bull*, 124, 372 –422. (1998).

12. Zirnsak, M., Moore, T. Saccades and shifting receptive fields: anticipating consequences or selecting targets? *Trends in cognitive sciences*, 18,12, 621-628. (2014)

13. Andersen, R. A., Mountcastle, V. B. The influence of the angle of gaze upon the excitability of the light-sensitive neurons of the posterior parietal cortex. *The Journal of Neuroscience*, 3(3), 532–548. (1983).

14. Kaiser, M., Lappe M. Perisaccadic mislocalization orthogonal to saccade direction. *Neuron*, 22;41(2), 293–300. (2004).

15. Zimmermann, E., Morrone, M. C., Burr, D. C. Visual mislocalization during saccades sequences. *Exp Brain Res*, 233(2):577-585. (2014).

16. Walker, R., McSorley, E., Haggard, P. The control of saccade trajectories: direction of curvature depends on prior knowledge of target location and saccade latency. *Percept Psychophys*, 68(1), 129-138. (2006).

17. Harmony, T. The functional significance of delta oscillations in cognitive processing. *Frontiers in Integrative Neuroscience*, 7, 83. (2013).

18. Fries, P. A mechanism for cognitive dynamics: neuronal communication through neuronal coherence. *Trends in Cognitive Sciences,* 9(10), 474–480. (2005).

19. Dowiasch, S., Blohm, G., Bremmer, F. Neural correlate of spatial (mis-)localization during smooth eye movements. *The European Journal of Neuroscience*, 44(2), 1846–1855. (2016).

20. Ross, J., Morrone, M.C., and Burr, D.C. Compression of visual space before saccades. *Nature*, 386, 598–601. (1997).

21. Neupane, S., Guitton, D., and Pack, C. C. (2016). Two distinct types of remapping in primate cortical area V4. *Nat. Commun*.7:10402.

22. Lamont P., Wiseman R. (1999). *Magic in Theory*. Hartfield: Hermetic Press.

23. Porter, T. C. Contributions to the study of flicker II. *Proceedings of the Royal Society of London Series A*, 70, 313–329. (1902).

24. Humphries, D., Driver, P. Protean defence by prey animals. *Oecologia*, 5 285–302. (1970).

25. Furuichi, N. Dynamics between a predator and a prey switching two kinds of escape motions. *J Theor Biol*, 217(2):159-66. (2002).

26. Szinte, M., Jonikaitis, D., Rangelov, D., Deubel, H. (2018). Pre-saccadic remapping relies on dynamics of spatial attention. *eLife*, **7**:e37598.

27. Rolfs, M., Jonikaitis, D., Deubel, H., and Cavanagh, P. (2011). Predictive remapping of attention across eye movements. *Nat. Neurosci*. 14, 252–256.

28. Arkesteijn, K., Belopolsky, A. V., Smeets, J., Donk, M. The Limits of Predictive Remapping of Attention Across Eye Movements. *Frontiers in psychology*, 10, 1146. (2019).

29. Botev, Z. I., Grotowski, J. F., Kroese, D. P. Kernel density estimation via diffusion. *Annals of Statistics*, 38:2916–2957. (2010).

30. Crossland, M.D., Sims, M., Galbraith, R.F., Rubin, G.S. Evaluation of a new quantitative technique to assess the number and extent of preferred retinal loci in macular disease. *Vision Research*, 44(13), 1537-1546. (2004).

31. Ludwig, C. J. H., Gilchrist, I. D. Measuring saccade curvature: A curve-fitting approach. *Behavior Research Methods, Instruments, & Computers*, 34, 618-624. (2002).

32. Nandy, A. S., Nassi, J. J., Reynolds, J. H. Laminar Organization of Attentional Modulation in Macaque Visual Area V4. *Neuron*, 4;93(1), 235-246. (2017).

33. Tass, P., Rosenblum, M.G., Weule, J., Kurths, J., Pikovsky, A., Volkmann, J., Schnitzler, A., Freund, H. J. Detection of n:m Phase Locking from Noisy Data: Application to Magnetoencephalography. *Physical review letters,* 81, 3291-3294. (1998).

34. Bowman, A.W., Azzalini, A. *Applied Smoothing Techniques for Data Analysis: the Kernel Approach with S-Plus Illustrations* (Oxford University Press, Oxford, 1997).

ACKNOWLEDGEMENTS

I would like to thank D. P. Melcher and S. Wirth for comments on the manuscript and B. Wichterlová for editing the manuscript. I would also like to thank A. S. Nandy for his guidance on the experimental design.

COMPETING INTEREST

Authors has no competing financial interest.

DATA AVAILABILITY

The data that supports this study is available upon reasonable request.

CODE AVAILABILITY

The custom Matlab code that supports the analyses reported in this study is available upon reasonable request.

SUPPLEMENTAL TEXT

Fig 1. Behavioural protocol. (A) Markers in the illustration of visual space show all retinotopic locations at which a probe was flashed before and after the deployment of attention, saccade planning, and, finally, the execution of a saccade. Probes of interest, presented along the tangential axes, are conspicuously highlighted in open circle markers. **(B)** Temporal sequence of a valid trial across experiments with respect to target onset.

Fig 2. Behavioural data. (A) Probability density map of foveal gaze and saccade landing was calculated using a bivariate gaussian kernel along with their bivariate contour ellipse area estimates for each probability density map. Error estimates are standard error of means across observers. **(B)** Shifts in peri-saccadic sensitivity along tangential axes with respect to target onset; error estimates were calculated using a 20-fold jackknife procedure. **(C)** Mean saccade trajectory deviation for horizontal and oblique saccades across experiments. Positive values on the ordinate denote trajectory deviation towards a clockwise location (cw), while negative values denote trajectory deviation towards a counterclockwise location (ccw) (*16*).

Fig 3. Frequency domain representation of peri-saccadic sensitivity and cross-location phase coherence estimates. (A-C) Representation of raw detrended peri-saccadic sensitivity at less and more eccentric locations in visual space. Shuffled (n=1000, dashed line) versus unshuffled (solid line) data set were used to compute location-specific spectral signatures at a $p<0.05$. For parafoveal and peripheral clockwise and counterclockwise locations a cross-location phase coherency analysis was performed.

Fig 4. Model architecture and neurobiological force field with simulated putative population sensitivity. (A) For illustration purposes, a single eccentricity dependent population receptive field (pRF) within a retinotopic field is highlighted in pink. A pRF is defined by its center, size, and an eccentric dependent population elastic field (pEF). **(B)** MGα denotes gaze transitional signals modelled as a virtual mass at infinity located in the direction of an upper tangential location approximating the initial shift in gaze. MF denotes compressive signals modelled as a varying mass located at a lower tangential location in the fovea. **(C)** Simulation results in the foveal region when a pRF is under the influence of a resultant force exerted by (i) MF and MGα (curved space, thick marker) (ii) MC (convergent signals modelled as a varying mass at a stationary peripheral site; see Methods) and (iii) MT (saccade transitional signals modelled as a virtual mass at infinity located in the direction of a straight saccade; see Methods). **(D)** A pRF bounded by pEF is highlighted in pink for parafoveal simulations. **(E)** MGβ denotes gaze translational signals modelled as a virtual mass at infinity located in the direction of a downward shifts in gaze, MM denotes a varying mass at a mislocalized peripheral target, and MS denotes the curved transitional signals modelled as a virtual mass at infinity located in the direction of a curvilinear saccade. **(F)** Curved, convergent and translational simulation results.

402

403 **Extended Data Fig. 1 Peri-saccadic spatiotemporal retinotopic shifts for foveal simulations.**

404 **(A)** hexagonal retinotopic field spanning the entire visual field. Retinotopic shifts are produced

405 by the perturbation of pRFs under an inverse force field in discrete time increments of 1ms by

406 the combination of external forces exerted by **(B)** corresponding masses ($M_{G\alpha}$ +M_F).

407

408 **Extended Data Fig. 2 Peri-saccadic spatiotemporal retinotopic shifts for parafoveal**

409 **stimulations. (A)** Retinotopic shifts when the combination of external forces is exerted by **(B)**

410 corresponding masses ($M_{G\beta}$ +M_M + M_S).

411

412 **METHODS**

413 **Human subjects**

414 Six consenting human subjects (5 females and 1 male; 21-26 years old) with corrected-to-normal

415 visual acuity participated in the three experiments reported. Three of the six subjects participated

416 in the foveal and parafoveal experiments. The remaining three subjects participated in the

417 peripheral experiment. The Yale Ethics Review board approved the protocol of these experiments

418 and the storage of the data that was collected.

419

420 **Visual stimuli and experimental protocol**

421 Fig. 1 summarizes the protocol used across experiments. In a dimly lit room, stimuli were

422 presented on a gamma corrected display with a spatial resolution of 1400 x 1050 pixels and a mean

423 luminance of 38cd/m^2. Eye movements were recorded using an infrared video-based eye-tracker

424 sampled at 1kHz (I-Scan Inc., Woburn, MA). While tightly head fixed using a head rest and a

customized bite bar, subjects at the onset of each trial acquired fixation for 300ms. Fixation within this temporal window was spatially aligned with the fixation point (0.5 dva in diameter) using a custom-developed 9-point eye-calibration procedure in Picto. Next, depending on the subject, a saccade target was presented at an eccentricity of 10° and at azimuth angles of 0° (for s_1), 45° (for s_2) and 315° (for s_3) (Fig. 1A). Following target onset, fixation was maintained for another 300-600ms within ~2dva fixation tolerance window, at the end of which the fixation spot was extinguished, which served as the central motor cue for subjects to make an eye movement towards the saccade target. For another 500ms after the central motor cue, the saccade target remained visible. Finally, a low contrast probe (at a contrast level which the subject could detect with 50% accuracy) were isotropically flashed, depending on the experiment, for 20ms either along the radial or tangential axis at a random time during the 300-600ms window between the target onset and the central motor cue (25% of trials) or at a random time between 0-340ms after the central motor cue (50% of the trials). On the remaining 25% (which yielded a false alarm rate of 1.2%), no probes were presented. All three conditions were randomly interleaved across trials. With respect to target onset, the presentation of flashed probes fell within a time window of 0-1285ms after target onset (Fig. 1B). Subject was asked to report, using a push button, whether they were able to detect the flashed probe. While the responses along the radial axis were not analyzed, the presentation of these probes was crucial in controlling for any response biases that may have emerged at upper or lower locations along tangential axes. To ensure that attentional and oculomotor resources was not being driven by an asymmetric stimuli configuration as it is the case in previous studies (*26, 27, 28*), no secondary salient spatial cue was presented. Along the tangential axes, a total of ~6010 trials were collected across experiments, with a minimum of 650 trials per subject.

448

449 **Statistical analyses**

450 To investigate gaze dynamics, probability density maps and variance estimates were calculated
451 using median filtered edge preserving fixational data, which was rotated to an angle of 0° across
452 target locations. Next, I calculated a gaze probability density map for the foveal and periphery
453 regions using a bivariate Gaussian kernel (*29*). The estimated locus of gaze across subjects was
454 defined as the peak of each probability density map (i.e., the yellow contour lines). To compare
455 the distribution of gaze in the fovea during the 0 to 209ms window after target onset versus 210 to
456 820ms window after target onset, a Mann-Whitney U statistic was calculated at p value less than
457 0.05. Further, variance in gaze was calculated using a bivariate Contour Ellipse Area (BCEA)
458 approach which included 68% of fixational data around the mean (*30*). Accompanying error bars
459 were obtained which denote the standard error of the mean variance across subjects. To investigate
460 the extent saccade trajectories were curved across experiments at each saccade location. Horizontal
461 and vertical eye positions, with the time window starting point constituting the moment fixation
462 was maintained to the moment the eye landed in the periphery, was isolated. Next to obtain a
463 measurement of curvature, the curved area that emerged from the eye position during this time
464 window was calculated. To then obtain a ratio measure of curvature per unit amplitude, this area
465 was divided by the amplitude of the saccade (*31*). Accompanying calculated error bars denote the
466 standard error of the mean at each target location across experiments. To investigate normalized
467 changes in peri-saccadic sensitivity across subjects, I first binned each subject's percent correct
468 responses for the foveal (Exp. 1), parafoveal (Exp. 2), and peripheral (Exp. 3) experiments, using
469 a 15ms sliding window that was moved in 45ms increments. Next, I obtained each subject's raw
470 peri-saccadic sensitivity, using a 20-fold jackknife procedure by estimating sensitivity from 95%

471 of the data. This was repeated 20 times, each time leaving out 5% of the data. This produced a
472 mean and an error estimate of peri-saccadic sensitivity at each tangential location for each
473 experiment across subjects (*32*). To control for any eccentric-dependent effect on raw peri-
474 saccadic sensitivity, these traces were normalized by the average sensitivity over the initial 100ms
475 in the data. To investigate frequency domain and cross-location phase coherence dynamics, a fast
476 Fourier transform (FFT) was applied to the detrended raw peri-saccadic sensitivity data. Next, we
477 computed the mean of the spectral signatures and corresponding standard error of the mean across
478 subjects. To than assess whether the observed periodicities were location specific, we randomly
479 shuffled (n=1000) the probe location identities across trials and calculated the sensitivity function
480 and periodicity of the shuffled data using the same procedures noted above. A two tailed paired-
481 sample t-test at p-values of 0.05 was calculated to assess the significance between shuffled and
482 non-shuffled data. Finally, for the cross-location phase coherence analysis, we applied an approach
483 to the shuffled and non-shuffled detrended data that is commonly used in assessing the underlying
484 coherence in neural data (*33*). I then projected the difference between phase angles of each subject
485 between counterclockwise (ccw) and clockwise (cw) locations and then calculated the resultant
486 vector across subjects.
487
488 **Novel computational framework - Retinotopic mechanics**
489 The underlying architecture of this simple mechanical model is composed of a retinotopic field
490 (ϕ_r) and a retinotopic lever which is inspired by a neurobiological force field. The retinotopic field
491 is a two-dimensional overlapping hexagonal grid of eccentricity-dependent receptive fields - $\mathrm{RF_i}$
492 - that tiled the foveal, parafoveal and peripheral regions in visual space (Extended Fig. 1-2). Each
493 $\mathrm{RF_i}$ was defined by three parameters: (a) p_i, the spatial extent of the RF center (x_i, y_i) at $\mathrm{t_0}$ (when

there is no resultant force acting on the ϕ_r). p_i determines the eccentricity - e_i of $\mathrm{RF_i}$, (b) s_i, the radius of $\mathrm{RF_i}$ is proportional to e_i, and (c) the movement extent (M_{max}) of $\mathrm{RF_i}$ is its $\mathrm{EF_i}$ which is also proportional to e_i. ϕ_r emerged from peri-saccadic attentional and oculomotor signals actively modulated by visually transient error signals that act as input and output forces of retinotopic lever in this field, and transiently perturb a constellation of population receptive fields from equilibrium and thereby modulate their putative population sensitivity (density readouts) as a function of space and time. For simulations at the less eccentric ("foveal"), the resultant force ($\overrightarrow{\mathrm{F_{R1}}}$) included an input and output force ($\overrightarrow{\mathrm{F_I}}$, and $\overrightarrow{\mathrm{F_O}}$) and an internal force ($\overrightarrow{\mathrm{F_E}}$) which $\mathrm{RF_i}$ at $\mathrm{t_{0+n}}$ experiences:

$$\overrightarrow{\mathrm{F_O}} = \overrightarrow{\mathrm{U_{M_{G\alpha}}}} \,.\, \mathrm{M_{G\alpha}} \,.\, |\mathrm{G\alpha}|$$

$$\overrightarrow{\mathrm{F_I}} = \overrightarrow{\mathrm{U_{M_F}}} \,.\, \mathrm{M_F} \,.\, \mathrm{R}_\beta^\varepsilon$$

$$\overrightarrow{\mathrm{F_{R1}}} = \overrightarrow{\mathrm{F_I}} \,.\, \mathrm{k_I} + \overrightarrow{\mathrm{F_O}} + \overrightarrow{\mathrm{F_E}}$$

where $\mathrm{M_{G\alpha}}$ and $\mathrm{M_F}$ are the virtual mass at infinity in the upward direction which approximates an initial shift in gaze and a foveal mass located at a lower tangential foveal retinotopic site which approximates a compressed shift in gaze respectively. $\overrightarrow{\mathrm{U_{M_{G\alpha}}}}$ and $\overrightarrow{\mathrm{U_{M_F}}}$ are the unit vectors in the direction of the virtual mass and the foveal mass respectively. $|\mathrm{G\alpha}|$ is the magnitude in gaze towards the upper tangential foveal retinotopic site, while R_β is the spatial difference between $\mathrm{RF_i}$ and $\mathrm{M_F}$ raised to an epsilon scalar – ε. The value of ε, depending on the retinotopic mechanics that best explains the phenomenon in question, can either be consistent with a proportional-distance rule (i.e., >0) or an inverse-distance rule (i.e., <0). Further, $\mathrm{k_I}$ was obtained by calculating the average of $\mathrm{R}_{\beta 0}^\varepsilon$ across $\mathrm{RF_i}$'s and then taking its reciprocal $\frac{1}{\left(\mathrm{R}_{\beta 0}^\varepsilon\right)}$, while $\overrightarrow{\mathrm{F_E}}$ is proportional to

the movement of RF_i. For the more eccentric ("parafoveal") simulations, the resultant force ($\overrightarrow{F_{R2}}$) included an input, output, an additional orthogonally biased translational force ($\overrightarrow{F_I}$, $\overrightarrow{F_O}$ and $\overrightarrow{F_T}$) and an internal force ($\overrightarrow{F_E}$) which RF_i at t_{0+n} experiences:

$$\overrightarrow{F_I} = \overrightarrow{U_{M_\beta}} \,.\, M_{G\beta} \,.\, |G\beta|$$

$$\overrightarrow{F_O} = \overrightarrow{U_{M_M}} \,.\, M_M \,.\, R_\mu^\varepsilon$$

$$\overrightarrow{F_T} = \overrightarrow{U_{M_S}} \,.\, M_S \,.\, |S|$$

$$\overrightarrow{F_{R2}} = \overrightarrow{F_O} \,.\, k_O + \overrightarrow{F_I} + \overrightarrow{F_T} + \overrightarrow{F_E}$$

where $M_{G\beta}$ and M_M are the virtual mass at infinity in the direction towards lower foveal tangential retinotopic site which approximates a complete compression of gaze and the mislocalized mass located at a peripheral retinotopic site that approximates a mislocalized saccade target respectively. $\overrightarrow{U_{M_{G\beta}}}$ and $\overrightarrow{U_{M_M}}$ are the unit vectors in the direction of the virtual mass and the mislocalized peripheral mass respectively. $|G\beta|$ is the magnitude of a fully compressed gaze which is roughly proportional to the magnitude of a mislocalized target. R_μ is the spatial difference between RF_i and M_M raised to ε, while $|S|$ approximates the magnitude of an impending saccade. The same calculation used to obtain k_I was used to obtain k_O, however in this case, the average of $R_{\mu 0}^\varepsilon$ across RF_i's was used. Depending on the stimulation, a time varying resultant force ($\overrightarrow{F_{R1}}$ or $\overrightarrow{F_{R2}}$) perturbed each RF_i, which produced spatiotemporal peri-saccadic retinotopic displacements (Extended Data Fig. 1-2). The population movements of the constellations of RF_i's manifested in time-varying modulation of raw density, modeling each RF_i as a bivariate gaussian kernel function *G*. A probability density estimate (or putative population sensitivity readouts), $\hat{f}$, was obtained using the following equation:

$$G\,(u) = \frac{1}{\sqrt{2\pi}} e^{-\frac{1}{2}u^{\mathrm{T}}u}$$

$$\hat{f}\,(\boldsymbol{x}, \mathbf{B}) = \frac{1}{k} \sum_{\mathrm{i}=1}^{\mathrm{k}} \mathrm{G}_{\mathbf{B}}\,(|\boldsymbol{x} - \boldsymbol{x_i}|)$$

Finally, population sensitivity readouts were later normalized using the same approach used to normalize the raw peri-saccadic sensitivity traces.

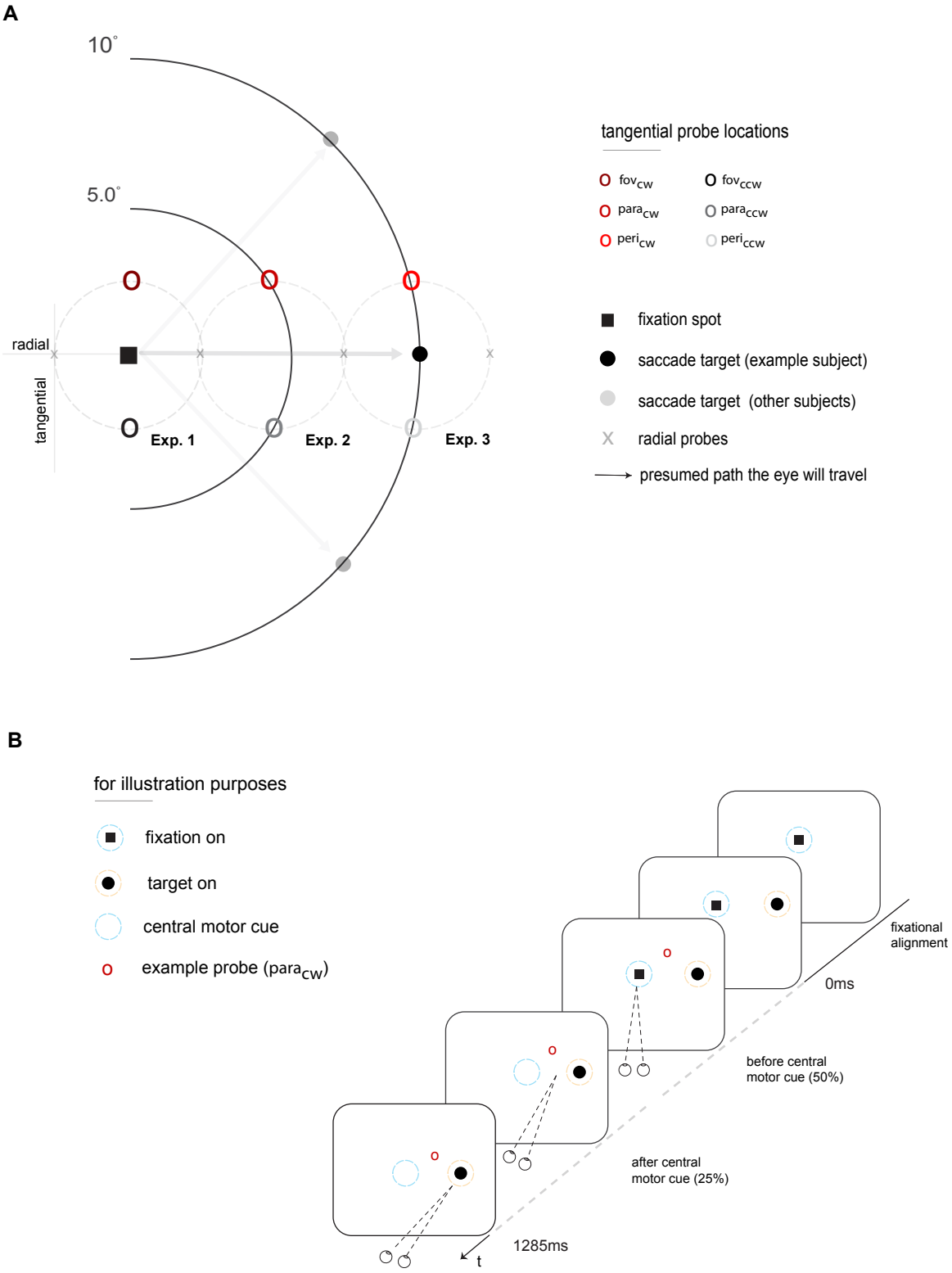

Fig 1. Behavioural protocol. (A) Markers in the illustration of visual space show all retinotopic locations at which a probe was flashed before and after the deployment of attention, saccade planning, and, finally, the execution of a saccade. Probes of interest, presented along the tangential axes, are conspicuously highlighted in open circle markers. **(B)** Temporal sequence of a valid trial across experiments with respect to target onset.

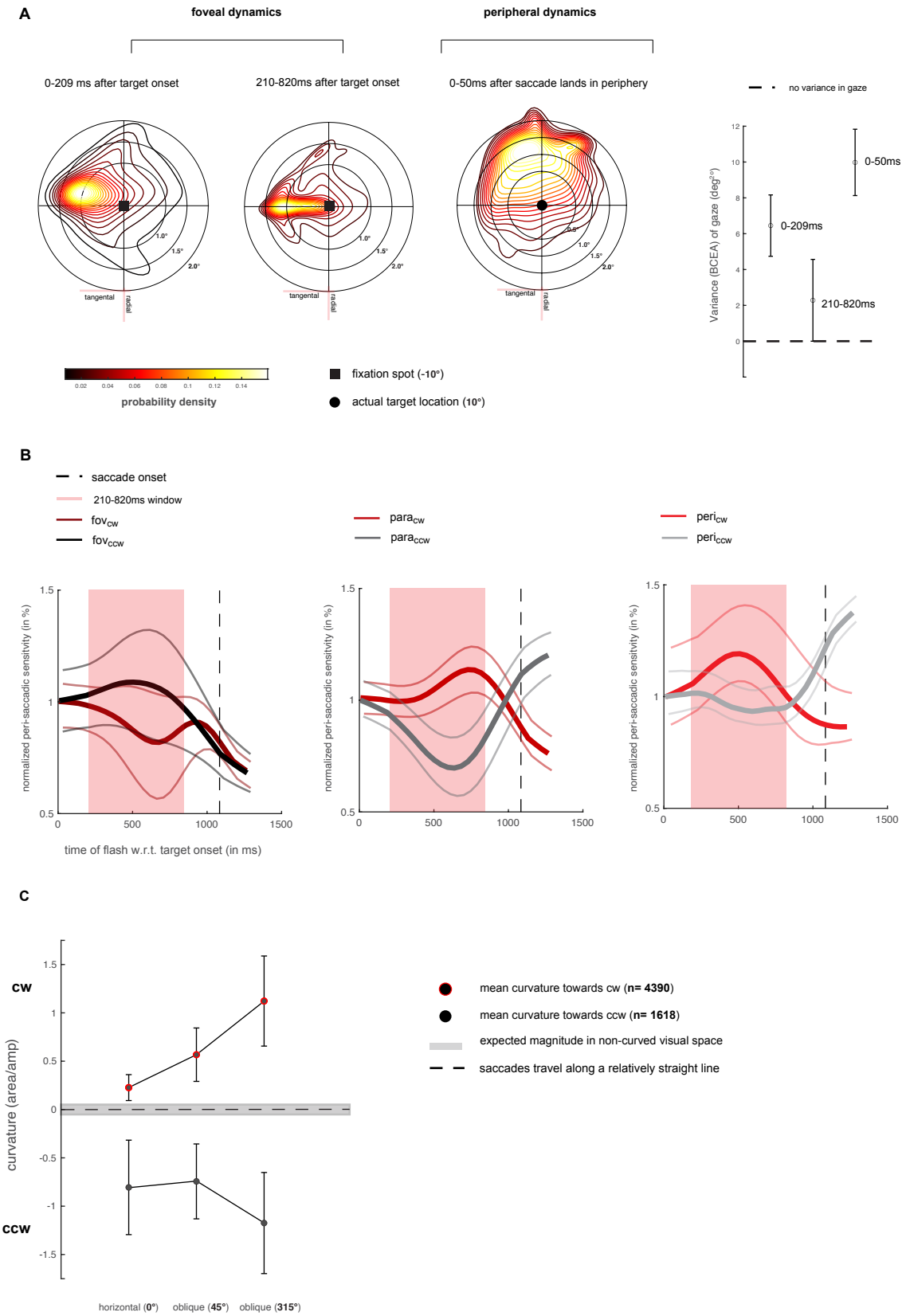

Fig 2. Behavioural data. (A) Probability density map of foveal gaze and saccade landing was calculated using a bivariate gaussian kernel along with their bivariate contour ellipse area estimates for each probability density map. Error estimates are standard error of means across observers. **(B)** Shifts in peri-saccadic sensitivity along tangential axes with respect to target onset; error estimates were calculated using a 20-fold jackknife procedure. **(C)** Mean saccade trajectory deviation for horizontal and oblique saccades across experiments. Positive values on the ordinate denote trajectory deviation towards a clockwise location (cw), while negative values denote trajectory deviation towards a counterclockwise location (ccw) (16).

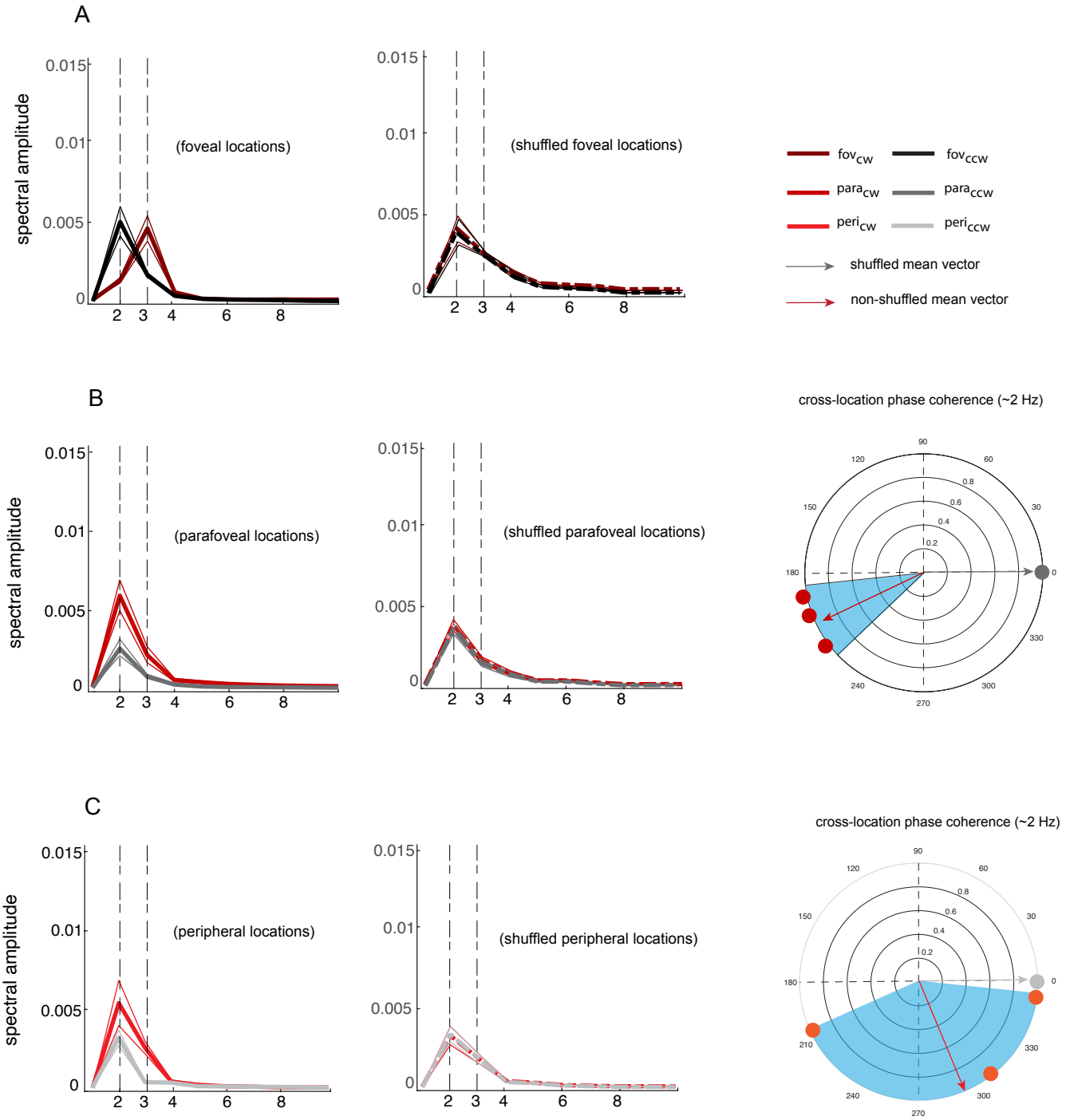

Fig 3. Frequency representation of peri-saccadic sensitivity and cross-location phase coherence. (A-C) Representation of raw detrended peri-saccadic sensitivity at less and more eccentric locations in visual space. Shuffled (n=1000, dashed line) versus unshuffled (solid line) data set were used to compute location-specific spectral signatures at a $p<0.05$. For parafoveal and peripheral clockwise and counterclockwise locations a cross-location phase coherency analysis was performed.

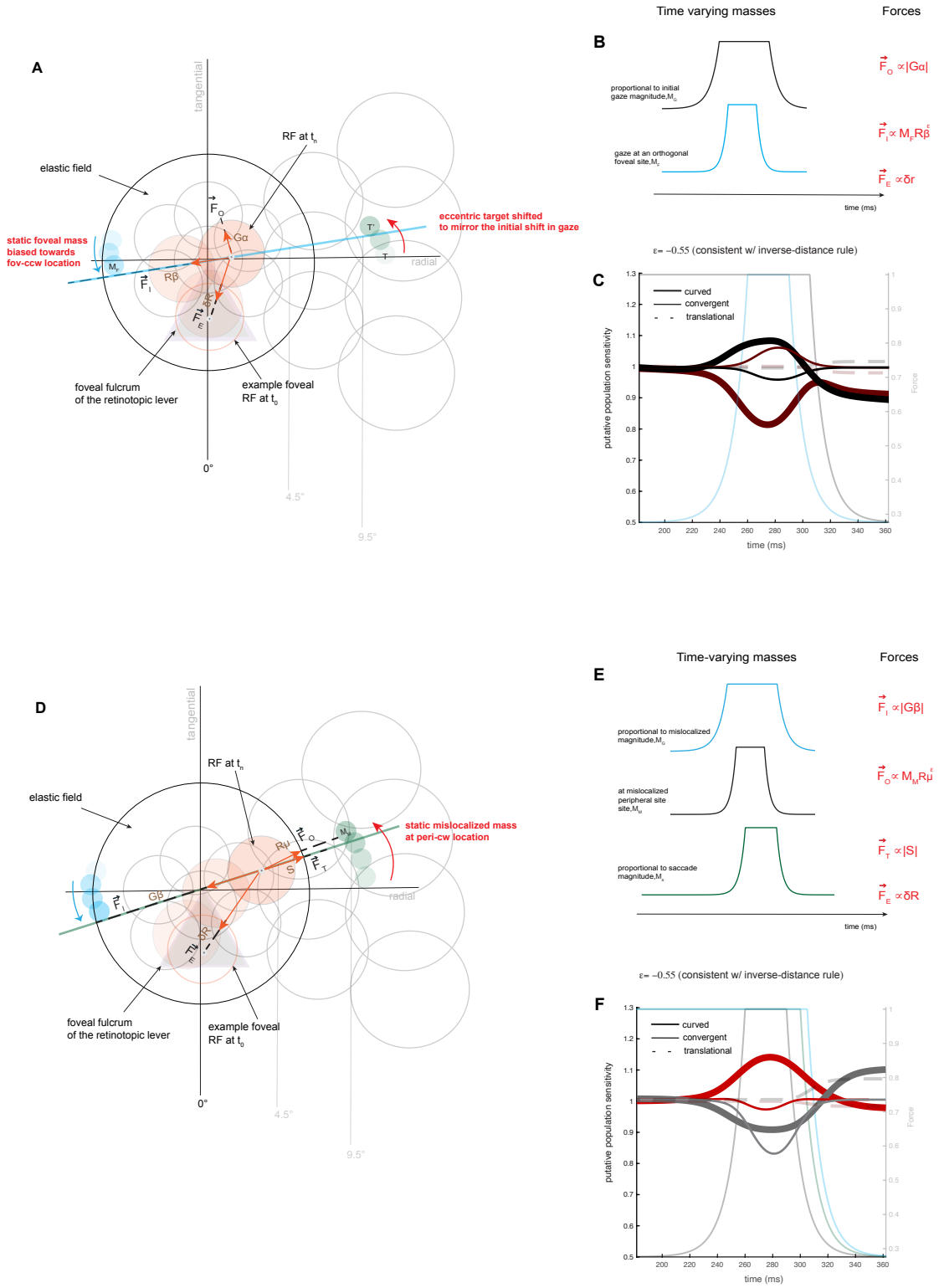

Fig 4. Model architecture and neurobiological force field with simulated putative population sensitivity. (A) For illustration purposes, a single eccentricity dependent population receptive field (pRF) within a retinotopic field is highlighted in pink. A pRF is defined by its center, size, and an eccentric dependent population elastic field (pEF). **(B)** $M_{G\alpha}$ denotes gaze transitional signals modelled as a virtual mass at infinity located in the direction of an upper tangential location approximating the initial shift in gaze. M_F denotes compressive signals modelled as a varying mass located at a lower tangential location in the fovea. **(C)** Simulation results in the foveal region when a pRF is under the influence of a resultant force exerted by (i) M_F and $M_{G\alpha}$ (curved space, thick marker) (ii) M_C (convergent signals modelled as a varying mass at a stationary peripheral site; see Methods) and (iii) M_T (saccade transitional signals modelled as a virtual mass at infinity located in the direction of a straight saccade; see Methods). **(D)** A pRF bounded by pEF is highlighted in pink for parafoveal simulations. **(E)** $M_{G\beta}$ denotes gaze translational signals modelled as a virtual mass at infinity located in the direction of a downward shifts in gaze, M_M denotes a varying mass at a mislocalized peripheral target, and M_S denotes the curved transitional signals modelled as a virtual mass at infinity located in the direction of a curvilinear saccade. **(F)** Curved, convergent and translational simulation results.